WEAK LENSING CALIBRATED M – T SCALING RELATION OF GALAXY GROUPS IN THE COSMOS FIELD[*]

K. Kettula[1], A. Finoguenov[1], R. Massey[4], J. Rhodes[2,3], H. Hoekstra[5], J. E. Taylor[6], P.F. Spinelli[7,8], M. Tanaka[9], O. Ilbert[10], P. Capak[11], H. J. McCracken[12], and A. Koekemoer[13]

Draft version September 17, 2013

ABSTRACT

The scaling between X-ray observables and mass for galaxy clusters and groups is instrumental for cluster based cosmology and an important probe for the thermodynamics of the intracluster gas. We calibrate a scaling relation between the weak lensing mass and X-ray spectroscopic temperature for 10 galaxy groups in the COSMOS field, combined with 55 higher mass clusters from the literature. The COSMOS data includes HST imaging and redshift measurements of 46 source galaxies per $arcmin^2$, enabling us to perform unique weak lensing measurements of low mass systems. Our sample extends the mass range of the lensing calibrated M–T relation an order of magnitude lower than any previous study, resulting in a power-law slope of $1.48^{+0.13}_{-0.09}$. The slope is consistent with the self-similar model, predictions from simulations, and observations of clusters. However, X-ray observations relying on mass measurements derived under the assumption of hydrostatic equilibrium have indicated that masses at group scales are lower than expected. Both simulations and observations suggest that hydrostatic mass measurements can be biased low. Our external weak lensing masses provides the first observational support for hydrostatic mass bias at group level, showing an increasing bias with decreasing temperature and reaching a level of 30–50 % at 1 keV.

Subject headings: cosmology: observations – galaxies: groups: general – gravitational lensing: weak

[1] University of Helsinki, Department of Physics, Gustaf Hällströmin katu 2a, FI-00014 Helsinki, Finland; kimmo.kettula@iki.fi

[2] California Institute of Technology, 1200 East California Boulevard, Pasadena, CA 91125, USA

[3] Jet Propulsion Laboratory, California Institute of Technology, Pasadena, CA 91109, USA

[4] Institute for Computational Cosmology, Durham University, South Road, Durham DH1 3LE, U.K.

[5] Leiden Observatory, Leiden University, Niels Bohrweg 2, NL-2333 CA Leiden, Netherlands

[6] Department of Physics and Astronomy, University of Waterloo, 200 University Avenue West, Waterloo, ON N2L 3G1, Canada

[7] Instituto de Astronomia, Geofísica e Ciências Atmosféricas (IAG),Rua do Matão, 1226 Cidade Universitária 05508-090, São Paulo, SP - Brazil

[8] Museu de Astronomia e Ciências Afins (MAST), Rua General Bruce, 586 Bairro Imperial de São Cristóvão 20921-030, Rio de Janeiro, RJ - Brazil

[9] National Astronomical Observatory of Japan, Osawa 2-21-1, Mitaka, Tokyo 181-8588, Japan

[10] LAM, CNRS-UNiv Aix-Marseille, 38 rue F. Joliot-Curis, 13013 Marseille, France

[11] Spitzer Science Center, 314-6 Caltech, 1201 E. California Blvd. Pasadena, CA 91125, USA

[12] Institut d'Astrophysique de Paris, UMR 7095, 98 bis Boulevard Arago, 75014 Paris, France

[13] Space Telescope Science Institute, 3700 San Martin Drive, Baltimore, MD 21218, USA

1. INTRODUCTION

As the largest gravitationally bound objects in the Universe, galaxy clusters and groups have proven to be important cosmological probes. They reside in the high-mass end of the cosmic mass function and have a formation history which is strongly dependent on cosmology. Thus the mass function of galaxy clusters and groups functions as an independent tool for constraining cosmological parameters.

Clusters and groups are now readily detected up to redshifts of unity and above through X-ray emission of hot intracluster gas [15], optical surveys of galaxies and the Sunyaev-Zel'dovich (SZ) effect in the millimeter range. The masses of these systems have typically been inferred through thermal X-ray emission or the velocity dispersion of galaxies. Both of these methods rely on the assumption of hydrostatic or gravitational equilibrium in the cluster or group, which is not always valid. Clusters and groups are found in a myriad of dynamical states and there is increasing evidence for non-thermal pressure support in the intracluster gas, skewing the mass estimates derived under the assumptions of a hydrostatic equilibrium (e.g. Nagai et al. 2007; Mahdavi et al. 2008; Shaw et al. 2010; Rasia et al. 2012; Mahdavi et al. 2013).

Fortunately, gravitational lensing has proven to be a direct way of measuring cluster and group masses regardless of the dynamical state or non-thermal pressure support in the system. In gravitational lensing the presence of a large foreground mass such as a galaxy cluster or group will bend the light radiating from a background source galaxy. In weak gravitational lensing the ellipticity of a source galaxy is modified, whereas strong lensing also produces multiple images of a single source. The weak lensing induced change in ellipticity is commonly referred to as shear. However, source galaxies typically have a randomly oriented intrinsic ellipticity, that is significantly larger than the lensing induced shear. Therefore the shear has to be averaged over a large sample of source galaxies in order to measure a weak lensing signal used to infer the mass of the lensing system.

The direct mass measurements methods described above are observationally expensive and not always applicable to low mass or high redshift systems. This has spurred the study of mass scaling relations for observables, which can be used as mass proxies. As X-ray observations have proven to be the most efficient way for constructing cluster and group catalogs, typically X-ray observables such as luminosity L_X, spectroscopic temperature T_X, and thermal energy of the intracluster gas $Y_X = T_X \times M_{gas}$ are used as mass proxies. Consequently, defining and calibrating these X-ray mass proxies is instrumental for cluster and group based cosmology.

The scaling between cluster or group temperature and mass is very fundamental. The simple self-similar model for cluster evolution developed by Kaiser (1986), which assumes pure gravitational heating of intracluster gas, predicts that cluster temperature is a direct measure of the total gravitational potential and thus mass of the system. The predicted scaling of mass to temperature is a power-law with a slope of 3/2. Deviations from the self-similar prediction can consequently be used to study non-gravitational physics affecting the gas.

Unfortunately, cluster and group masses are typically derived from X-ray observations under the assumption of hydrostatic equilibrium (HSE) regardless of dynamical state. Also, temperatures are usually derived from the same observation as hydrostatic masses, introducing possible covariance between the observed quantities. The hydrostatic M-T relations typically give power-law slopes in the range of $1.5 - 1.7$ (see Böhringer et al. 2012; Giodini et al. 2013, for summaries of recent literature). Notably, samples that only include higher-mass systems with temperatures above 3 keV tend to predict M-T relations that have a slope close to the self-similar prediction of 1.5, whereas samples including lower-mass systems tend to predict a slightly steeper proportionality.

The accuracy of the calibration of mass - temperature scaling can be significantly improved by using independent weak lensing cluster mass measurements. However, this type of studies have only been performed in the cluster mass regime by Smith et al. (2005); Hoekstra (2007); Okabe et al. (2010); Jee et al. (2011); Hoekstra et al. (2012); Mahdavi et al. (2013). The aim of this work is to calibrate the scaling between weak lensing masses and X-ray temperatures of the hot intracluster gas for a sample of galaxy groups in the COSMOS survey field. This work is an extension to Leauthaud et al. (2010), who investigated the scaling between weak lensing mass and X-ray luminosity in the same field.

This paper is organized as follows. We present the data and galaxy group sample used for our analysis in Sections 2 and 3, and give details on the X-ray and weak lensing analysis in Sections 4 and 5. We present the resulting M – T relation in Section 6, discuss our findings in Section 7, conclude and summarize our findings in Section 8. Throughout this paper we assume WMAP9 year cosmology (Hinshaw et al. 2012), with $H_0 = 70$ h_{70} km / s / Mpc, $\Omega_M = 0.28$ and $\Omega_\Lambda = 0.72$. All uncertainties are reported at a 68 % significance, unless stated otherwise.

2. COSMOS DATA

In this Section we briefly present the observations of the COSMOS survey field used for our analysis. The COSMOS survey consists of observations of a contiguous area of 2 square degrees with imaging at wavelengths from radio to X-ray and deep spectroscopic follow-up (see e.g. overview by Scoville et al. 2007).

2.1. Lensing catalog

The shear measurements of source galaxies are based on Hubble Space Telescope (HST) imaging of the COSMOS field using the Advanced Camera for Surveys (ACS) Wide Field Channel (WFC) (Scoville et al. 2007; Koekemoer et al. 2007). As the COSMOS field was imaged during 640 orbits during HST Cycles 12 and 13, the ACS/WFC imaging of the COSMOS field is the HST survey with the largest contiguous area to date. The derivation of shear measurement is described in detail by Leauthaud et al. (2007), Leauthaud et al. (2010), and Leauthaud et al. (2012). The shear measurement has been calibrated on simulated ACS images containing a known shear (Leauthaud et al. 2007), and we have

---

[15] with intracluster gas we refer to the intergalactic gas in both galaxy groups and clusters. We follow the convention of referring to those systems with mass lower than $\sim 10^{14}$ $M_\odot$ as groups and higher as clusters.

updated that with each subsequent improvement of the catalog.

The final weak lensing catalog contains accurate shape measurements of 272 538 galaxies, corresponding to approximately 46 galaxies per arcmin^2, and a median redshift of $z = 1.06$. 25 563 of the source galaxies have spectroscopic redshift measurements from the zCOSMOS program (Lilly et al. 2007), the remaining source galaxies have photometric redshifts measured using over 30 bands (Ilbert et al. 2009).

2.2. *X-ray group catalog*

The X-ray group catalog we used has been presented in George et al. (2011) and is available online. In brief, we used all XMM-Newton (described in Hasinger et al. 2007; Cappelluti et al. 2009) and Chandra observations (Elvis et al. 2009) performed prior to 2010 in catalog construction. Point source removal has been produced separately for Chandra and XMM before combining the data, as described in Finoguenov et al. (2009), producing a list of 200+ extended sources. We run a red-sequence finder to identify the galaxy groups following the procedure outlined in Finoguenov et al. (2010). Extensive spectroscopy available for the COSMOS field allowed a 90 % spectroscopic identification of the $z < 1$ group sample. George et al. (2012) explored the effect of centering by taking an X-ray center or the most massive group galaxy (MMGG).

Previously the X-ray group catalog has been used in Leauthaud et al. (2010) to calibrate the M – L relation. It has been shown there that there is a correlation between the level of X-ray emission and the significance of the weak lensing signal. In the current work we take advantage of the fact that the significance required to measure the mean X-ray temperature allows us to perform individual mass measurements, and although the sample size is much smaller when compared to the M – L relation, we do not need to stack several groups in order to produce the results. The high significance of the selected groups also has a much better defined X-ray centering.

3. SAMPLE SELECTION

We selected sources from the COSMOS X-ray group catalog (Section 2.2) with a detection significance of 10σ and above. As we choose to exclude cluster cores from temperature determination (see Section 4) and consequently only use regions with low scatter in pressure (Arnaud et al. 2010), our sample should be unaffected by selection bias.

Our initial sample contained 13 sources. However, we excluded the group with id number 6 because X-ray coverage was not sufficient to constrain the spectroscopic temperature. We further excluded the sources with id numbers 246 and 285, as they are located at the edge of the COSMOS field and thus fall outside the coverage of the HST observations (Section 2.1).

The remaining 10 sources in our sample all have a clear X-ray peak with a single optical counterpart and are free of projections (Finoguenov et al. 2007, XFLAG = 1). As our data allows us to extend our lensing analysis out to large radii, possible substructure in the central parts visible in X-rays is not relevant for our mass estimates. Instead, infalling subgroups at cluster outskirts are more

Table 1
Properties of the galaxy group sample.

id [a]	N_H [b] $[10^{20}$ cm$^{-2}]$	z	RA (J2000) [c] degrees	Dec (J2000) [c] degrees
11	1.80	0.220	150.18980	1.65725
17	1.78	0.372	149.96413	1.68033
25	1.75	0.124	149.85146	1.77319
29	1.74	0.344	150.17996	1.76887
120	1.80	0.834	150.50502	2.22506
149	1.77	0.124	150.41566	2.43020
193	1.69	0.220	150.09093	2.39116
220	1.71	0.729	149.92343	2.52499
237	1.70	0.349	150.11774	2.68425
262	1.84	0.343	149.60007	2.82118

[a] id number in the COSMOS X-ray group catalog (Section 2.2)
[b] The LAB weighted average galactic absorption column density (Kalberla et al. 2005)
[c] RA and DEC of the X-ray peak.

important. Based on our X-ray group catalog, we can rule out this kind of substructure at > 20–30 % level in mass.

We adopt the coordinates of the X-ray peaks as the locations of the group centers, but we also tested the effect of using the MMGG as a center in performing the lensing analysis (Section 5.3). The properties of the clusters in our sample are presented in Table 1. The deep X-ray coverage and high density of background galaxies with determined shear in the COSMOS field allows us to treat each system individually in our analysis.

4. X-RAY REDUCTION AND ANALYSIS

For the X-ray analysis we used EPIC-pn data from the XMM-Newton wide field survey of the COSMOS field (Hasinger et al. 2007) with the latest calibration information available in October 2012 and XMM Scientific Analysis System (SAS) release xmmsas_20120621_1321-12.0.1. We produced event files with the epchain tool and merged the event files of pointings which were within 10 arcmin of the adopted group center for each system. The merged event files were filtered, excluding bad pixels and CCD gaps and periods contaminated by flares, and including only events with patterns 0 – 4. We generated out-of-time event files, which we subsequently used to subtract events registered during pn readout.

We extracted spectra from an annulus corresponding to $0.1 - 0.5$ R$_{500}$ (see Table 2). As differences of a few 10 % in the inner and outer radii of the X-ray extraction region will be smeared out by the PSF, we determined R$_{500}$ from the virial radius in the X-ray group catalog (Section 2.2, based on the M-L relation of Leauthaud et al. 2010), assuming a halo concentration of 5. The groups were visually inspected for point sources, which we masked using a circular mask with a 0.5 arcmin radius. We grouped the spectra to a minimum of 25 counts per bin.

As the groups in the COSMOS field do not fill the FOV, we used the merged event files to extract local background spectra. We selected background regions using the criteria that they are located at a minimum distance of R$_{200}$ ($\sim$ 2–6 arcmin, determined from the X-ray group catalog Section 2.2) and a maximum distance of 10 arcmin from the adopted group center, and that they do not contain any detectable sources. The background spectra where used as Xspec background files in subse-
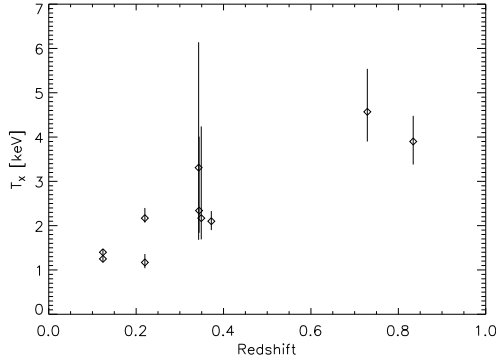
Figure 1. Plot showing X-ray temperature T_X vs redshift z of the COSMOS systems analyzed in this work.

quent spectral fits and thus subtracted from the data.

For X-ray spectroscopy we used an Xspec model consisting of an absorbed thermal APEC component in a 0.5–7.0 keV energy band, with solar abundance tables of Grevesse & Sauval (1998) and absorption cross-sections of Balucinska-Church & McCammon (1992). We fixed the metal abundance to 0.3 of the solar value, and used redshift and Galactic absorption column density values listed in Table 1. In order to account for spatial variation in the Galactic foreground, we included an additional thermal component with a temperature of 0.26 keV and solar abundance and found that the contribution from this component was negligible.

As the inner radii of the extraction regions is smaller than the EPIC-pn point spread function (PSF), some flux from the excluded central 0.1 R_{500} region might scatter to the extraction region. We accounted for this scatter by extracting spectra from the excluded central regions and fitting them with a similar model as described above. We estimated the scatter to the 0.1–0.5 R_{500} extraction regions using the best-fit model and added the contribution due to the scatter to our analysis. The core regions of groups with id numbers 29 and 220 did not posses a sufficient number of photons to fit a spectrum and we estimate that the scatter from the central region is negligible for these systems. For the remaining systems the fraction of flux in the extraction region scattered from the central region varies between 3 and 21 % (see Table 2).

We detected the thermal emission component in the 0.1 – 0.5 R_{500} region with a statistical significance of 3.2 – 24.5σ and best-fit temperatures in the range of 1.2 – 4.6 keV (see Fig. 1 and Table 2). Thus our sample extends the measurements of weak lensing based M – T relations to a lower temperature range than previous studies by a factor of four (Hoekstra 2007; Okabe et al. 2010; Jee et al. 2011; Mahdavi et al. 2013).

5. WEAK LENSING ANALYSIS

For our weak lensing analysis we used the COSMOS shear catalog.

5.1. Lensing signal

In our analysis we measured the lensing signal independently for each system in our sample in terms of azimuthally averaged surface mass density contrast $\Delta\Sigma(r)$. A spherically symmetric mass distribution is expected to induce a shear, which is oriented tangentially to the radial vector. This signal is also known as the E-mode. The cross-component shear, or B-mode signal, is angled at 45°from the tangential shear, and the azimuthally averaged value is expected to be consistent with zero for a perfect lensing signal.

The azimuthally averaged surface mass density contrast is related to the projected tangential shear of source galaxies γ_t by

$$\Delta\Sigma(r) = \overline{\Sigma}(<r) - \overline{\Sigma}(r) = \Sigma_{crit} \times \gamma_t(r), \qquad (1)$$

were $\overline{\Sigma}(<r)$ is the mean surface mass density within the radius r, $\overline{\Sigma}(r)$ is the azimuthally averaged surface mass density at radius r, and Σ_{crit} is the critical surface mass density. The critical surface mass density depends on the geometry of the lens - source system as

$$\Sigma_{crit} = \frac{c^2}{4\pi G} \frac{D_{OS}}{D_{OL} D_{LS}}. \qquad (2)$$

Here c is the speed of light, G Newton's gravitational constant and D_{OS}, D_{OL} and D_{LS} the angular diameter distances between observer and source, observer and lens, and lens and source, respectively.

For each lensing system, we selected the source galaxies from the COSMOS shear catalog with a projected distance of $0.1 - 4$ Mpc in the lens plane and a lower limit for the 68 % confidence interval for the photometric redshift higher than the redshift of the lensing system. Approximately 23 % of the source galaxies in the lensing catalog have secondary photometric redshift peaks. In order to avoid biasing mass estimates due to catastrophic outliers, we exclude these galaxies from our analysis.

The lensing signal might be diluted, if a significant number of group galaxies are scattered into the source sample. For instance, Hoekstra (2007) showed in Fig. 3 that the effect is modest for high mass clusters using ground based data ($\sim$ 20 % at R_{2500}). As our space based data is deeper, giving a larger number of sources, and we analyse low mass systems with a smaller number of member galaxies, the effect on our sample is significantly smaller. The effect is mainly limited to the central parts of the groups, which we cut out from our analysis. Furthermore, as our photometric redshifts are based on 30+ bands and we exclude source galaxies with secondary redshift peaks, our lensing masses are unaffected by contamination by group members.

We calculated the surface mass density contrast $\Delta\Sigma_{i,j}$ for each lens – source pair using Equations 1 and 2. For the computation of $\Delta\Sigma_{i,j}$, spectroscopic redshift was used instead of photometric redshift for those source galaxies where it was available. As we compute $\Delta\Sigma$ at radii greater than 0.1 Mpc, our lensing signals are largely unaffected by non-weak shear or contributions from the central galaxy (Leauthaud et al. 2010). As an illustration, we show the combined and binned tangential and cross-component lensing signals for all sources in the sample in Fig. 2.

The uncertainty of the observed tangential shear σ_{γ_t} is affected by the measurement error of the shape σ_{meas} and the uncertainty due to the intrinsic ellipticity of source galaxies σ_{int}, known as intrinsic shape noise. Leauthaud et al. (2007, 2010) estimated the intrinsic

Table 2
Results of the X-ray analysis.

id	0.1 R_{500} [a] arcmin	0.5 R_{500} [b] arcmin	T_X [c] keV	f_{scat} [d] %	sign. [e] σ	χ^2 [f]	degrees of freedom
11	0.35	1.77	$2.2^{+0.2}_{-0.1}$	5	24.5	273.42	263
17	0.19	0.96	$2.1^{+0.2}_{-0.2}$	21	18.2	96.36	91
25	0.37	1.87	$1.3^{+0.1}_{-0.1}$	3	11.8	139.40	121
29	0.18	0.89	$2.3^{+1.7}_{-0.5}$	...	3.2	24.75	26
120	0.13	0.67	$3.9^{+0.6}_{-0.5}$	10	16.6	66.49	69
149	0.42	2.08	$1.4^{+0.1}_{-0.1}$	4	19.1	123.95	132
193	0.20	1.02	$1.2^{+0.2}_{-0.1}$	14	3.9	27.54	23
220	0.16	0.79	$4.6^{+1.0}_{-0.7}$	...	15.8	43.49	32
237	0.20	0.99	$2.2^{+2.1}_{-0.5}$	12	5.3	24.99	26
262	0.21	1.03	$3.3^{+2.8}_{-1.6}$	5	5.7	40.14	33

[a] Inner radii of the extraction region
[b] Outer radii of the extraction region
[c] X-ray temperature of the group
[d] Fraction of the flux in the $0.1 - 0.5$ R_{500} region scattered from the central region
[e] Statistical significance of the thermal X-ray component
[f] χ^2 of the best-fit model

shape noise of source galaxies in the COSMOS shear catalog to $\sigma_{int} = 0.27$.

Nearby LSS can also contribute to the uncertainty of lensing mass estimates (Hoekstra 2001, 2003). For the COSMOS field, Spinelli et al. (2012) found that the LSS affects the shear measurements as an external source of noise, where the average contribution to the uncertainty of the tangential shear is $\sigma_{LSS} = 0.006$. Thus, the total uncertainty of the tangential shear measurements for each source galaxy can be approximated by:

$$\sigma_{\gamma_t}^2 \approx \sigma_{meas}^2 + \sigma_{int}^2 + \sigma_{LSS}^2, \qquad (3)$$

since the correlation between the terms σ_{meas} and σ_{LSS} is small, the correlation between σ_{int} and the other two terms vanishes. For this work we use $\sigma_{meas,j}$ from the updated Leauthaud et al. (2010) catalog, $\sigma_{int} = 0.27$ and $\sigma_{LSS} = 0.006$.
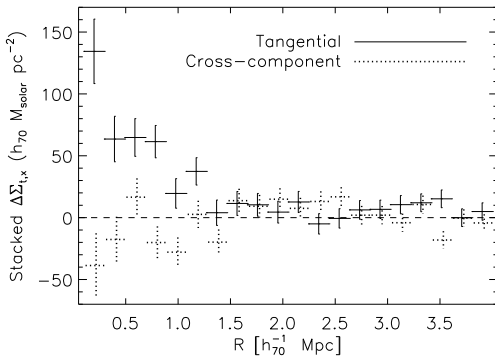
Figure 2. The stacked $\Delta\Sigma$ showing the total tangential (solid data) and cross-component (dotted data) lensing shear of all galaxy groups in the sample. Errors represent the total error given by Equation 3. The data are binned to 20 equally spaced bins in a radial range of 0.1 to 4 Mpc.

5.2. *Lensing mass estimates*

Numerical simulations indicate that the density profile of galaxy clusters or groups typically follow the Navarro–Frenk–White (NFW) profile (Navarro et al. 1997), given by

$$\rho\left(r\right) = \frac{\delta_c\,\rho_{cr}}{(r/r_s)\,(1+r/r_s)^2}. \qquad (4)$$

In this work we define total group mass as the mass inside which the mean NFW mass density $<\rho> = 200\,\rho_{cr}$, where ρ_{cr} is the critical density of the Universe at the group redshift z_d. We denote this mass by M_{200} and define it as $M_{200} \equiv M(r_{200}) = 200\rho_{cr}\frac{4}{3}\pi r_{200}^3$. The NFW concentration parameter $c_{200} = r_{200}/r_s$ gives the relation between r_{200} and the characteristic scale radius r_s. Finally, the density contrast in the NFW profile (Eq 4) is defined as

$$\delta_{c_{200}} = \frac{200}{3}\,\frac{c_{200}^3}{\ln(1+c_{200}) - \frac{c_{200}}{1+c_{200}}}. \qquad (5)$$

The analytic solution for the surface mass density contrast signal corresponding to a NFW profile $\Delta\Sigma_{NFW}$ is given by

$$\Sigma_{NFW}(x) = \begin{cases} \frac{2r_s\delta_c\rho_{cr}}{(x^2-1)}\left[1 - \frac{2}{\sqrt{1-x^2}}\mathrm{arctanh}\sqrt{\frac{1-x}{1+x}}\right] & x < 1, \\ \frac{2r_s\delta_c\rho_{cr}}{3} & x = 1, \\ \frac{2r_s\delta_c\rho_{cr}}{(x^2-1)}\left[1 - \frac{2}{\sqrt{x^2-1}}\arctan\sqrt{\frac{x-1}{1+x}}\right] & x > 1, \end{cases} \qquad (6)$$

where $x = R/r_s$ (e.g. Bartelmann 1996; Wright & Brainerd 2000; Kneib & Natarajan 2011). The solution depends on the mass, concentration parameter and redshift of the lensing system. For this work we assume that M_{200} and c_{200} are related by

$$c_{200} = \frac{5.71}{(1+z_d)^{0.47}}\left(\frac{M_{200}}{2.0\times10^2\,h^{-1}M_\odot}\right)^{-0.084} \qquad (7)$$

given by Duffy et al. (2008). We experimented with letting concentration vary freely, however the shear data did not allow for this extra degree of freedom. Thus as the redshifts of the systems in our sample are known, the only unknown in the solution of $\Delta\Sigma_{NFW}$ is mass M_{200}.

We estimated the masses by fitting $\Delta\Sigma_{NFW}$ to the measured $\Delta\Sigma$ (Section 5.1), in a radial range of 0.1–4 Mpc. The data were not binned for the fit. We used the Metropolis-Hastings Markov Chain Monte Carlo algorithm for χ^2 minimization (see Fig. 3 and Fig. 4) and found best-fit M_{200} in the range of ~ 0.3–6×10^{14} h_{70}^{-1} $M_\odot$ (see Fig. 5 and Table 3). This mass range is consistent with the low X-ray temperatures described above.

5.3. Centering comparison

George et al. (2012) (see also Hoekstra et al. 2011) showed that miscentering the dark matter halo can bias the lensing mass of the halo low. Therefore we investigated the effects of the uncertainty of the centering of the dark matter halo on our lensing mass estimates by performing the weak lensing analysis described above with centering on the locations of the X-ray peaks and MMGGs (from George et al. 2011), and comparing the resulting halo masses.

The offset between the MMGGs and X-ray peaks are typically less than the uncertainty of the position of the X-ray centroid, which is given by 32 arcsec divided by the signal-to-noise ratio (~ 10–15 for our sample) for XFLAG=1 groups in the COSMOS group catalog (see Fig. 6). The only exceptions are groups with X-ray id# 149 and 220, which have an offset of 43 and 59 arcsec respectively.

The best-fit M_{200} using MMGG and X-ray centering are typically consistent within a few per cent (Table 3 and Fig. 6). The only deviant group is X-ray id# 220, which has a MMGG centered mass $\sim 20\%$ lower than the X-ray centered. This system has a peculiar S-shape morphology, which makes accurate center determination difficult (Guzzo et al. 2007). However, the mass discrepancy with MMGG and X-ray centering is at a less than 1σ statistical significance (see also Section 5.5 for further discussion on the this system).

A miscentered cluster is expected to show a suppression in the lensing signal at small scales. We do not detect this effect in the mass surface density contrast profiles (Fig. 4), including the two groups with significant offsets between MMGG and X-ray centers. We thus conclude that the chosen X-ray centers are accurate and that our lensing masses are not significantly affected by uncertainties in centering.

5.4. Bias due to M–c relation

A possible systematic in the lensing analysis is an incorrect assumed mass – concentration relation for the NFW profile (Eq. 7). E.g. Hoekstra et al. (2012) showed that varying the normalisation of the M–c relation by $\pm$ 20 % biases lensing NFW mass estimates by ~ 5–15 %, depending on the mass definition. However, the sensitivity of NFW mass estimates to possible biases in the M–c relation diminishes when the mass estimates are extended further from the cluster center.

Our lensing masses are measured within R_{200} and they are consistent with the stacked lensing analysis of galaxy groups in the COSMOS field by Leauthaud et al. (2010), who used the M-c relation of Zhao et al. (2009) instead of the Duffy et al. (2008) relation used by us. Furthermore, the mass range implied by both our lensing analysis and the lensing analysis of Leauthaud et al. (2010) is consistent with the typical dark matter halo mass derived with clustering analysis in the COSMOS field (Allevato et al. 2012). An incorrect assumed NFW concentration would result in lensing masses contradicting the clustering analysis.

5.5. Massive galaxy group at z = 0.73

Guzzo et al. (2007) performed a weak lensing analysis of the massive galaxy group at redshift z = 0.73 in the COSMOS field, with id #220 in the X-ray group catalog. They reported a very high weak lensing mass of $6 \pm 3 \times 10^{15}$ $M_\odot$ for the dark matter halo, which is in apparent tension with the X-ray mass $M_{500} \simeq 1.6 \times 10^{14}$ $M_\odot$ derived from their X-ray spectroscopic temperature $T_X = 3.51^{+0.60}_{-0.46}$ keV using M-T relations from the literature.

Our X-ray spectroscopic temperature of $4.6^{+1.0}_{-0.7}$ keV is consistent with the X-ray analysis of Guzzo et al. (2007). However, we found a weak lensing M_{200} of $4.12^{+1.41}_{-1.23} \times 10^{14}$ $M_\odot$ (scaled to $h = 1.0$ as used by Guzzo et al. 2007). This is over an order of magnitude lower than the lensing mass of Guzzo et al. (2007), but consistent within errors with the mass predictions from X-ray analyses. This implies that the previously reported high lensing mass is the total mass of the whole superstructure, whereas the lower mass implied by both X-rays and our lensing analysis is the mass of the galaxy group. This argument is further supported by the clustering analysis of groups in the COSMOS field (see Section 5.4 and Allevato et al. 2012). We further note that exclusion of this source from our sample would not affect our results.

6. M–T SCALING RELATION

We used our center excised X-ray temperatures and weak lensing group masses in the COSMOS field (Table 2 and 3) to calibrate the scaling relation between these two quantities. As the systems in our sample have both low mass and temperature, we are probing a largely unexplored region of the mass – temperature plane.

In the self-similar model cluster and group mass and temperature are related by a power-law

$$M \times E(z) = N \times T_X^\alpha. \qquad (8)$$

with slope $\alpha = 3/2$ (Kaiser 1986). Here $E(z)$, defined as

$$E(z) = \frac{H(z)}{H_0} = \sqrt{\Omega_M (1+z)^3 + \Omega_\lambda} \qquad (9)$$

for flat cosmologies, describes the scaling of overdensity with redshift.

Scaling relations at galaxy group masses are typically derived for M_{500} (e.g. Finoguenov et al. 2001; Sun et al. 2009; Eckmiller et al. 2011), i.e. the mass inside the radius where the average density is 500 times the critical density of the Universe. We rescaled the lensing masses derived above to this value using the best-fit NFW profiles to enable direct comparison. We assumed the power-law relation given by Eq. 8 and linearised it by taking a

Table 3
Results of the weak lensing analysis.

id	M_{500} [a] 10^{14} h_{70}^{-1} $M_\odot$	M_{200} [a] 10^{14} h_{70}^{-1} $M_\odot$	c_{200} [b]	χ^2 [c]	degrees of freedom [d]	MMGG / X-ray centering ratio [e]
11	$1.28^{+0.14}_{-0.06}$	$1.79^{+0.20}_{-0.09}$	4.74	25762.57	22571	$1.03^{+0.39}_{-0.34}$
17	$0.92^{+0.52}_{-0.42}$	$1.31^{+0.73}_{-0.59}$	4.38	12749.11	10960	$1.00^{+0.56}_{-0.45}$
25	$0.20^{+0.19}_{-0.14}$	$0.27^{+0.26}_{-0.18}$	6.42	73753.62	64811	$1.00^{+0.94}_{-0.67}$
29	$0.93^{+0.44}_{-0.36}$	$1.31^{+0.62}_{-0.51}$	4.48	19686.50	16968	$0.99^{+0.47}_{-0.39}$
120	$0.60^{+1.00}_{-0.58}$	$0.92^{+1.51}_{-0.88}$	3.22	5122.80	4296	$1.00^{+1.65}_{-0.96}$
149	$0.97^{+0.34}_{-0.30}$	$1.33^{+0.47}_{-0.41}$	5.38	103367.55	91433	$0.99^{+0.163}_{-0.32}$
193	$0.25^{+0.25}_{-0.18}$	$0.34^{+0.33}_{-0.24}$	5.75	47237.02	41059	$1.01^{+0.98}_{-0.71}$
220	$3.76^{+1.29}_{-1.12}$	$5.88^{+2.01}_{-1.75}$	2.85	7443.86	6108	$0.80^{+0.33}_{-0.28}$
237	$0.63^{+0.36}_{-0.29}$	$0.88^{+0.50}_{-0.41}$	4.70	21859.89	19021	$1.06^{+0.47}_{-0.50}$
262	$0.82^{+0.47}_{-0.37}$	$1.15^{+0.66}_{-0.52}$	4.54	10039.91	8546	$1.01^{+0.57}_{-0.45}$

[a] centered on the X-ray peak
[b] halo concentration of the best-fit NFW profile given by the mass-concentration relation in Eq 7
[c] χ^2 of the best-fit model
[d] the number of source galaxies in the weak lensing analysis for each system is given by the degrees of freedom + 1
[e] the ratio of M_{200} centered on the MMGG to M_{200} centered on the X-ray peak, see Section 5.3

logarithm

$$\log_{10} \frac{M_{500}E(z)}{10^{14}h_{70}^{-1}} = \log_{10} N + \alpha \times \log_{10} \frac{T_X}{3keV}. \quad (10)$$

We evaluated the logarithm of the normalization and the slope of the M – T relation using the FITEXY linear regression method, with bootstrap resampling to compute statistical uncertainties of the fit parameters.

For the COSMOS systems, we obtained the best-fit parameters $\alpha = 1.71^{+0.57}_{-0.40}$ and $\log_{10} N = 0.39^{+0.04}_{-0.10}$, with $\chi^2 = 5.07$ for 8 degrees of freedom (see Table 4, Fig. 7 and 8). However, as all our systems have low masses and large errors, the constraint on the scaling relation suffers from rather large uncertainties.

We therefore extended our sample with additional measurements at higher temperatures/masses. Hoekstra et al. (2011) determined weak lensing masses for a sample of 25 moderate X-ray luminosity clusters drawn from the 160 square degree survey (160SD Vikhlinin et al. 1998; Mullis et al. 2003), using HST ACS observations. Unfortunately X-ray temperatures are available for only 5 systems, which we use here. To extend the mass range further we also include measurements for 50 massive clusters that were studied as part of the Canadian Cluster Comparison Project (CCCP). The lensing masses, based on deep CFHT imaging data, are presented in Hoekstra et al. (2012), whereas the X-ray temperatures are taken from Mahdavi et al. (2013). The X-ray temperatures in Mahdavi et al. (2013) are obtained with both Chandra and XMM-Newton, but Chandra temperatures are adjusted to match XMM-Newton calibration.

This gives us a total sample of 65 systems with masses and temperatures spanning the range of a few times 10^{13} to a few times 10^{15} $M_\odot$ and 1–12 keV. Fitting the $M_{500} - T_X$ relation to the whole extended sample we obtained the best-fit parameters $\alpha = 1.48^{+0.13}_{-0.09}$ and $\log_{10} N = 0.34^{+0.02}_{-0.04}$ with $\chi^2 = 112.57$ for 63 degrees of freedom (see Table 4, Fig. 7 and 8).

We evaluated intrinsic scatter of the relation by making a distribution of the ratio of data to best-fit model for each point and computing the dispersion. The resulting scatter in mass at fixed T for the relation fitted to COSMOS data points and to the full sample are consistent, 28 ± 13 % and 28 ± 7 % respectively, indicating that the samples are consistent with each other.

7. DISCUSSION

The slope of our best-fit relation of the full sample $1.48^{+0.13}_{-0.09}$ is consistent with the self-similar prediction of 3/2 (Kaiser 1986). Unfortunately direct comparison of our best-fit relation to most other weak lensing calibrated M–T relations is not possible. Okabe et al. (2010) calibrated deprojected center excised temperatures (whereas our temperatures are projected) to M_{500} for the LoCuSS cluster sample, consisting of only cluster mass systems, and attained a slope of 1.49 ± 0.58. Hoekstra (2007) and Jee et al. (2011) calibrated X-ray temperatures to weak lensing M_{2500} for cluster mass systems and attained slopes of $1.34^{+0.30}_{-0.28}$ and 1.54 ± 0.23 respectively. As their mass definition differs from ours and masses are thus derived from a smaller region, their relations are not directly comparable to our analysis. In the case of Jee et al. (2011) the clusters are also at a significantly higher redshift than our sample, representing a cluster population at an earlier evolutionary stage.

However, Mahdavi et al. (2013) used the 50 CCCP clusters, which are also included in our sample, to fit scaling relations between X-ray observables and lensing masses. For M_{500}–T_X scaling they obtained a slope of 1.97 ± 0.89 and 1.42 ± 0.19 with a scatter in mass of 46 ± 23 % and 17 ± 8, using R_{500} derived from weak lensing and X-ray analysis respectively. Both of these are consistent within the errorbars with our findings.

The fact that the published lensing calibrated M–T relations at cluster masses and our group mass predict consistent slopes, indicates that both clusters and groups follow the same mass-to-temperature scaling. This is in apparent tension with relations relying on HSE mass es-
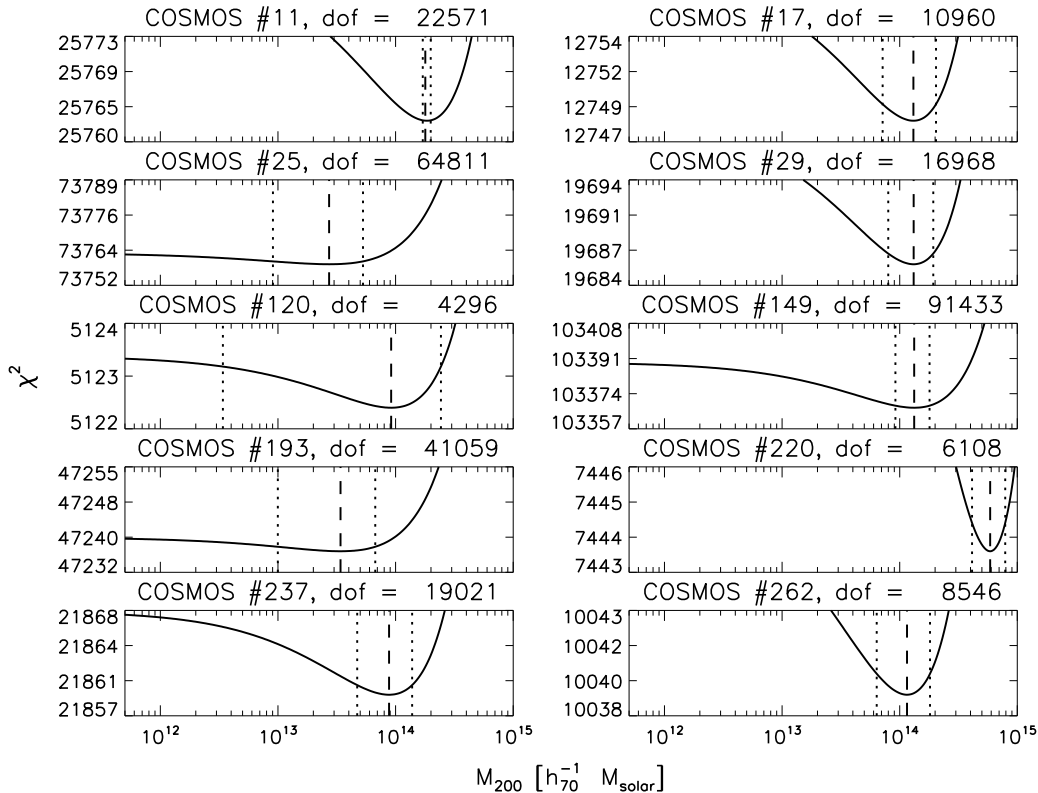
Figure 3. Plot of the χ^2 as a function of mass for NFW profile fits to azimuthally averaged mass surface density contrast. The dashed vertical line shows the best-fit M_{200}, dotted lines indicate the 1σ confidence intervals of M_{200}.

Table 4
Best-fit parameters of the $M_{500} - T_X$ scaling relation.

Sample	Slope α	Normalisation $\log_{10} N$	Intrinsic scatter %	χ^2	degrees of freedom
COSMOS	$1.71^{+0.57}_{-0.40}$	$0.39^{+0.04}_{-0.10}$	28 ± 13	5.07	8
COSMOS+CCCP+160SD	$1.48^{+0.13}_{-0.09}$	$0.34^{+0.02}_{-0.04}$	28 ± 7	112.57	63
COSMOS+CCCP+160SD, modified T_X	$1.40^{+0.12}_{-0.10}$	$0.32^{+0.02}_{-0.03}$	35 ± 9	117.99	63

timates, which generally predict steeper slopes and lower normalisation when group mass systems are included (see Fig 9). E.g. Finoguenov et al. (2001) used ASCA observations of the extended HIFLUGCS sample consisting of 88 systems spanning a similar mass and temperature range as our full sample and obtained a slope of 1.636 ± 0.044 for the $M_{500} - T_X$ relation, Sun et al. (2009) calibrated a similar relation to archival Chandra observations of 43 groups and 14 clusters and obtained a slope of 1.65 ± 0.04, and Eckmiller et al. (2011) obtained a slope of 1.75 ± 0.06 for a sample consisting of 112 groups and HIFLUGCS clusters. However, e.g. Vikhlinin et al. (2009) used a sample of clusters with $T_X \gtrsim 2.5$ keV to calibrate a M_{500}–T_X relation under the assumption of HSE, and obtained a slope of 1.53 ± 0.08, consistent with our weak lensing relations.

The difference in slope between hydrostatic and our weak lensing calibrated M–T relation is significant at ∼ 1–2σ level (see Fig. 10). The steeper slope and lower normalisation of HSE relations amounts to a temperature dependent bias between the scaling relations at an up to ∼ 2σ significance (see Fig. 9, lower panel).

Simulations indicate that HSE masses may be biased low due to non-thermal pressure support and kinetic pressure from gas motion (e.g. Nagai et al. 2007; Shaw et al. 2010; Rasia et al. 2012). Furthermore, the deviation from self-similarity in the M–T relation implied by HSE mass estimates is hard to reproduce in simulations (Borgani et al. 2004). Thus the preferred interpretation is a deviation between hydrostatic and lensing masses, amounting to ∼ 30–50 % at 1 keV. Our study provides the first observational support for this scenario at group scales. This effect has previously been observed at cluster masses by Mahdavi et al. (2008) and Mahdavi et al. (2013).

The effect of deviation between hydrostatic and lensing masses on scaling relations has previously been studied by Nagai et al. (2007). They simulated a sample of groups and clusters in a mass range approximately consistent with our extended sample, including effects
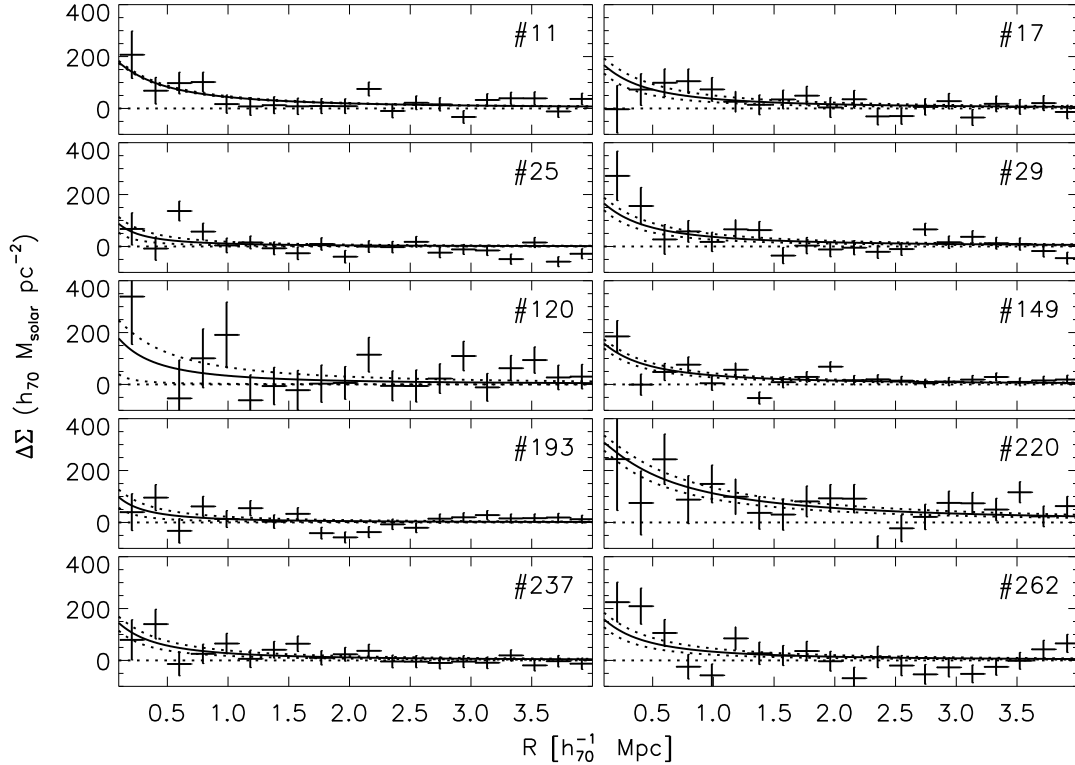
Figure 4. Azimuthally averaged mass surface density contrast $\Delta\Sigma$ profiles of the individual systems used for the weak lensing analysis. The profile is measured in a radial range of $0.1 - 4$ Mpc. Data show the measured $\Delta\Sigma$, solid lines show the $\Delta\Sigma$ of the best-fit NFW density profiles while the dotted lines indicate the statistical uncertainty of the fitted profiles. The profile fits are performed to un-binned data, here the data are binned to 20 equally spaced radial bins for plot clarity.
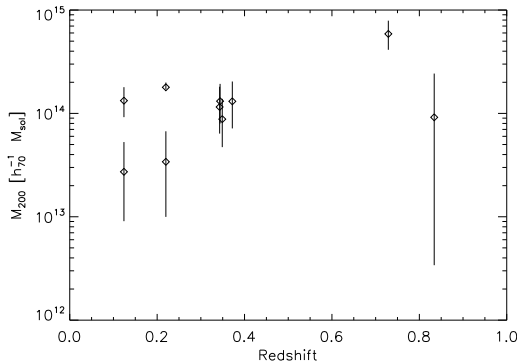
Figure 5. Plot showing weak lensing mass M_{200} v.s. redshift z of the COSMOS systems analyzed in this work.

Figure 6. Plot showing the ratio of lensing mass estimates for COSMOS galaxy groups centering on the most massive group galaxies (MMGGs) to mass estimates centering on the locations of the X-ray peaks v.s. the offset between the location of MMGGs and X-ray peaks.

of cooling and star formation. The simulated clusters were used for mock Chandra observations to calibrate an M_{500}–T_X relation using both true masses and masses derived under the hydrostatic equilibrium condition. Their best-fit relation using true masses is consistent with our lensing relation whereas their hydrostatic relation very accurately follows the observed hydrostatic relation of Sun et al. (2009) (see Fig 9 and 10). This provides further evidence that a bias in hydrostatic masses can affect the shape of scaling relations.

7.1. X-ray cross-calibration

Cross-calibration issues in the energy dependence of the effective area of X-ray detectors affects cluster spectroscopic temperatures obtained with different instruments (e.g. Snowden et al. 2008; Nevalainen et al. 2010; Kettula et al. 2013; Mahdavi et al. 2013). Recent observations indicate cluster temperatures measured with Chandra are typically ~ 15 % higher than those measured with XMM-Newton (Nevalainen et al. 2010; Mahdavi et al. 2013). As we compare our lensing calibrated M-T relation relying on XMM-Newton temperature measurements (or Chandra temperatures modified to match XMM-Newton) to Chandra based relations in literature, we investigate here if the detected discrepan-
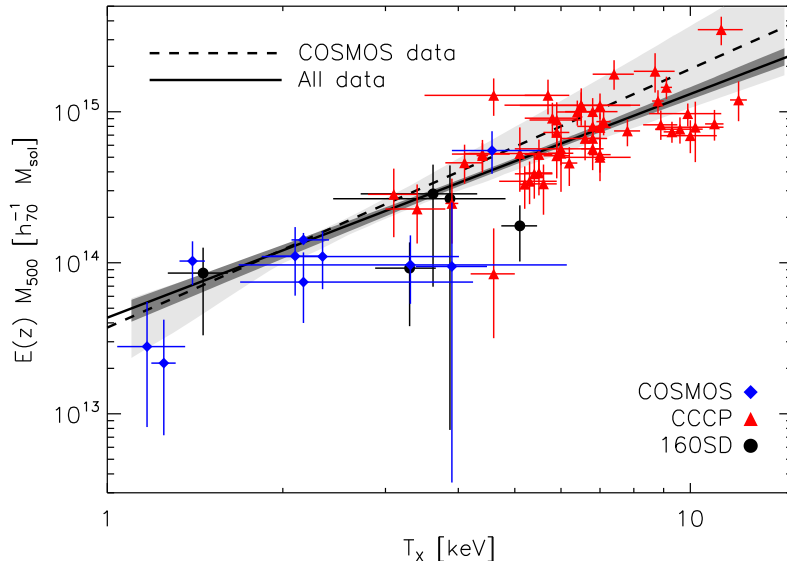
Figure 7. The scaling of cluster mass M_{500} to X-ray temperature T_X. Blue diamonds show COSMOS systems analyzed in this work, red triangles are systems from the CCCP cluster catalog and black circles are from the 160SD survey. The solid line and dark shaded region shows the best-fit scaling relation with statistical uncertainties fitted to all data points, the dashed line and light shaded region shows the relation fitted to COSMOS data points.
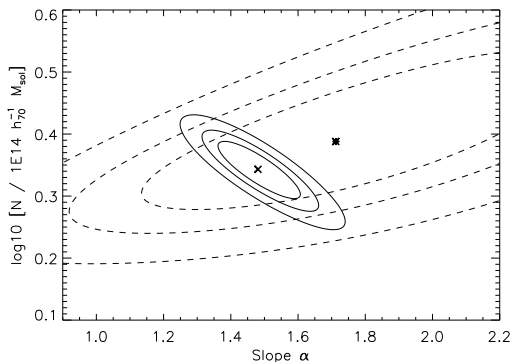
Figure 8. Likelihood contours at 68, 90 and 99 % statistical significance for the parameters of the $M_{500} - T_X$ scaling relation fitted to COSMOS systems described in this work (dashed contours) and to all data points shown in Fig. 7 (solid contours).

cies can be attributed to X-ray cross-calibration uncertainties.

Whereas cluster temperatures $\gtrsim 4$ keV are typically inferred from the shape of the bremsstrahlung continuun which depends strongly on the energy dependence of the effective area, lower group temperatures are mainly determined from emission lines and are thus independent of energy dependent cross-calibration. This effect is seen in comparisons of group and cluster temperatures obtained with XMM-Newton and Chandra (Snowden et al. 2008). As the measured energy of a photon at the detector also depends on the redshift of the source, we use the temperature and redshift dependent modification given by

$$T_X^{\mathrm{modified}} = T_X^{\mathrm{XMM}} \times \left(1 + \frac{0.15 \, T_X^{\mathrm{XMM}}}{10\mathrm{keV}} \frac{1}{1+z}\right) \quad (11)$$

to modify our XMM-Newton based temperatures to match Chandra calibration (see Fig 11).

Re-fitting the M_{500}–T_X relation with the modified

XMM temperatures, we find a marginally flatter slope than using unmodified temperatures. The slope still consistent with the self-similar prediction of $3/2$ (Table 4, and Fig. 10 and 12). Comparing to Chandra based HSE relations from literature, we find that HSE still predicts lower masses at group scales than lensing. We conclude that the differences between HSE and lensing M-T relations can not be explained by X-ray cross-calibration uncertainties and that lensing calibrated relations have slopes consistent with self-similarity for both Chandra and XMM-Newton based temperatures.

8. SUMMARY AND CONCLUSIONS

We calibrated a scaling relation between weak lensing masses and spectroscopic X-ray temperatures for a sample of 10 galaxy groups in the COSMOS field, 5 clusters from the 160SD survey, and 50 clusters from the CCCP survey. This gave a sample of 65 systems, spanning a wide mass and temperature range of $M_{500} \sim 10^{13}$–10^{15} $M_\odot$ and $T_X \sim$1–12 keV, extending weak lensing calibrated M–T relations to an unexplored region of the mass – temperature plane.

We found that the best-fit slope of the relation is consistent with the prediction for self-similar cluster evolution of Kaiser (1986). This is in apparent tension with M–T relations at group scales in literature, which use X-ray masses derived under HSE. These relations typically predict steeper slopes and lower normalizations.

The deviations from self-similarity implied by HSE relations are likely due to HSE masses being biased low in comparison to unbiased lensing masses. We find that the bias increases with decreasing temperature, amounting to ~30–50 % at 1 keV. This effect has been detected in simulations and our study provides the first observational evidence for it at group scales. We also show that this effect is not a product of cross-calibration issues between X-ray detectors.

We conclude that this work demonstrates the impor-
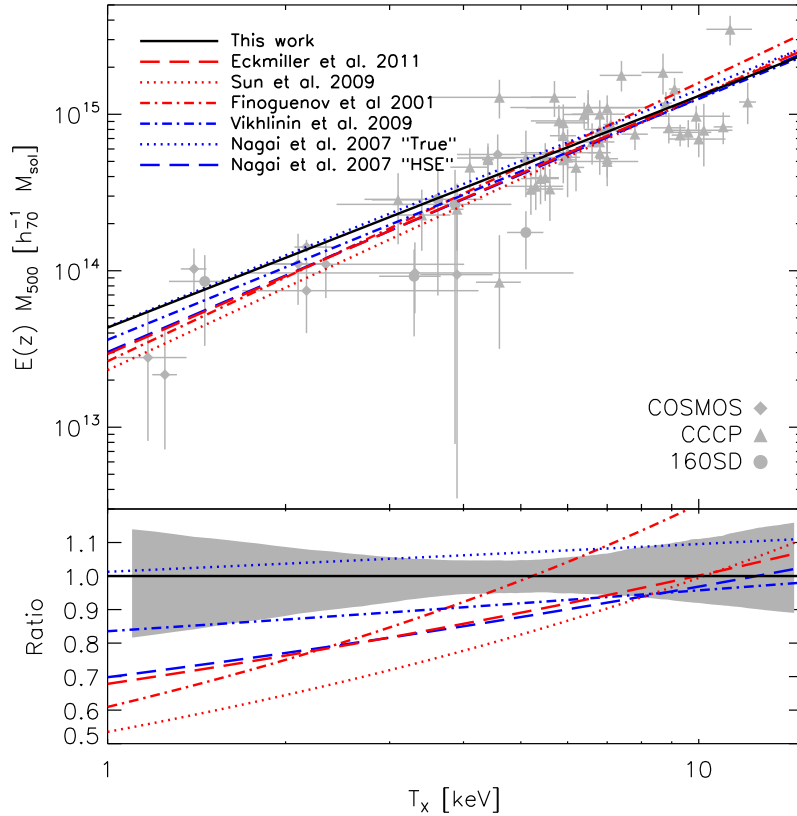
Figure 9. *Top panel:* Comparison of $M_{500} - T_X$ relations discussed in the text. The solid line corresponds to the best-fit weak lensing calibrated relation combining COSMOS, CCCP and 160SD samples in this work, data points are shown in gray. *Bottom panel:* Ratio of $M_{500} - T_X$ relations shown in the top panel to the best-fit relation in this work (solid line). Gray shaded region shows the relative statistical uncertainty of our relation.
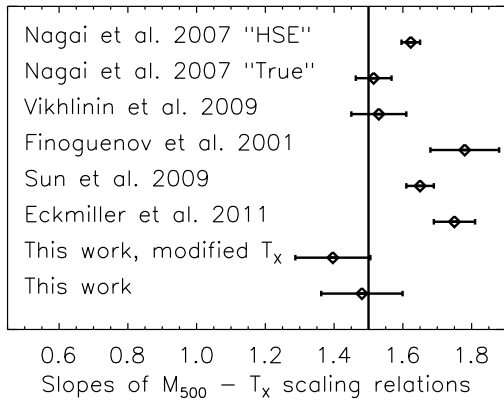
Figure 10. Comparison of the slopes of $M_{500} - T_X$ relations shown in Fig. 9 and Fig. 12. The vertical line corresponds to the self-similar slope of 3/2, the error bars describe the 68 % statistical uncertainties of the slopes.

tance of unbiased weak lensing calibrated scaling relations for precision cosmology with galaxy clusters and groups. Although costly, more weak lensing surveys of galaxy groups are needed to extend the statistical analysis of this work.
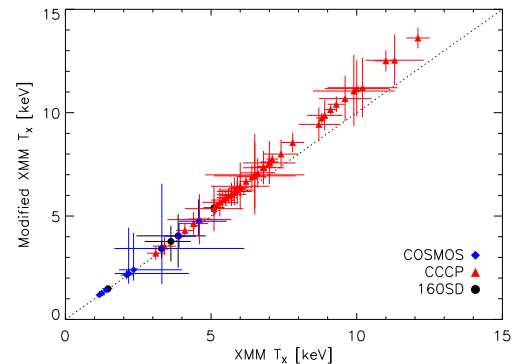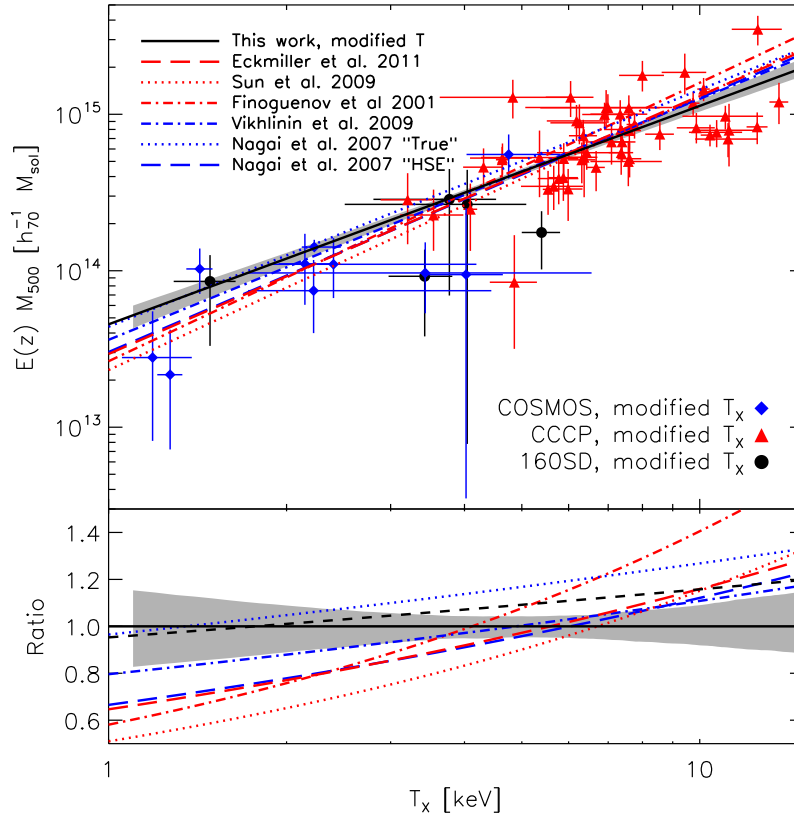
Figure 11. Plot showing XMM-Newton X-ray temperatures modified for Chandra calibration v.s. unmodified XMM-Newton temperatures for our group and cluster sample.

REFERENCES

Allevato, V., Finoguenov, A., Hasinger, G., et al. 2012, ApJ, 758, 47

Figure 12. *Top panel:* The solid line and shaded region shows $M_{500} - T_X$ relation and statistical uncertainties using the XMM-Newton temperatures modified for Chandra calibration, with comparison to other relations discussed in the text. *Bottom panel:* Ratio of the relations shown in the top panel to the relation fitted data with XMM-Newton temperatures modified for Chandra calibration (solid line). The shaded region shows the relative statistical uncertainty of the modified XMM relation.

Arnaud, M., Pratt, G. W., Piffaretti, R., et al. 2010, A&A, 517, A92

Balucinska-Church, M., & McCammon, D. 1992, ApJ, 400, 699

Bartelmann, M. 1996, A&A, 313, 697

Böhringer, H., Dolag, K., & Chon, G. 2012, A&A, 539, A120

Borgani, S., Murante, G., Springel, V., et al. 2004, MNRAS, 348, 1078

Cappelluti, N., Brusa, M., Hasinger, G., et al. 2009, A&A, 497, 635

Duffy, A. R., Schaye, J., Kay, S. T., & Dalla Vecchia, C. 2008, MNRAS, 390, L64

Eckmiller, H. J., Hudson, D. S., & Reiprich, T. H. 2011, A&A, 535, A105

Elvis, M., Civano, F., Vignali, C., et al. 2009, ApJS, 184, 158

Finoguenov, A., Watson, M. G., Tanaka, M., et al. 2010, MNRAS, 403, 2063

Finoguenov, A., Connelly, J. L., Parker, L. C., et al. 2009, ApJ, 704, 564

Finoguenov, A., Guzzo, L., Hasinger, G., et al. 2007, ApJS, 172, 182

Finoguenov, A., Reiprich, T. H., Bohringer, H. 2001, A&A, 368, 749

George, M. R., Leauthaud, A., Bundy, K., et al. 2012, ApJ, 757, 2

George, M. R., Leauthaud, A., Bundy, K., et al. 2011, ApJ, 742, 125

Giodini, S., Lovisari, L., Pointecouteau, E., et al. 2013, Space Sci. Rev., 177, 247

Grevesse, N., & Sauval, A. J. 1998, Space Sci. Rev., 85, 161

Guzzo, L., Cassata, P., Finoguenov, A., et al. 2007, ApJS, 172, 254

Hasinger, G., Cappelluti, N., Brunner, H., et al. 2007, ApJS, 172, 29

Hinshaw, G., Larson, D., Komatsu, E., et al. 2012, arXiv:1212.5226

Hoekstra, H., Mahdavi, A., Babul, A., & Bildfell, C. 2012, MNRAS, 427, 1298

Hoekstra, H., Donahue, M., Conselice, C. J., McNamara, B. R., & Voit, G. M. 2011, ApJ, 726, 48

Hoekstra, H. 2007, MNRAS, 379, 317

Hoekstra, H. 2003, MNRAS, 339, 1155

Hoekstra, H. 2001, A&A, 370, 743

Ilbert, O., Capak, P., Salvato, M., et al. 2009, ApJ, 690, 1236

Jee, M. J., Dawson, K. S., Hoekstra, H., et al. 2011, ApJ, 737, 59

Kaiser, N. 1986, MNRAS, 222, 323

Kalberla, P. M. W., Burton, W. B., Hartmann, D., et al. 2005, A&A, 440, 775

Kettula, K., Nevalainen, J., & Miller, E. D. 2013, A&A, 552, A47

Kneib, J.-P., & Natarajan, P. 2011, A&A Rev., 19, 47

Koekemoer, A. M., Aussel, H., Calzetti, D., et al. 2007, ApJS, 172, 196

Leauthaud, A., Tinker, J., Bundy, K., et al. 2012, ApJ, 744, 159

Leauthaud, A., Finoguenov, A., Kneib, J.-P., et al. 2010, ApJ, 709, 97

Leauthaud, A., Massey, R., Kneib, J.-P., et al. 2007, ApJS, 172, 219

Lilly, S. J., Le Fèvre, O., Renzini, A., et al. 2007, ApJS, 172, 70

Mahdavi, A., Hoekstra, H., Babul, A., et al. 2013, ApJ, 767, 116

Mahdavi, A., Hoekstra, H., Babul, A., & Henry, J. P. 2008, MNRAS, 384, 1567

Mullis, C. R., McNamara, B. R., Quintana, H., et al. 2003, ApJ, 594, 154

Nagai, D., Kravtsov, A. V., & Vikhlinin, A. 2007, ApJ, 668, 1

Navarro, J. F., Frenk, C. S., & White, S. D. M. 1997, ApJ, 490, 493

Nevalainen, J., David, L., & Guainazzi, M. 2010, A&A, 523, A22

Okabe, N., Zhang, Y.-Y., Finoguenov, A., et al. 2010, ApJ, 721, 875

Rasia, E., Meneghetti, M., Martino, R., et al. 2012, New Journal of Physics, 14, 055018

Shaw, L. D., Nagai, D., Bhattacharya, S., & Lau, E. T. 2010, ApJ, 725, 1452

Smith, G. P., Kneib, J.-P., Smail, I., et al. 2005, MNRAS, 359, 417

Scoville, N., Abraham, R. G., Aussel, H., et al. 2007, ApJS, 172, 38

Scoville, N., Aussel, H., Brusa, M., et al. 2007, ApJS, 172, 1

Snowden, S. L., Mushotzky, R. F., Kuntz, K. D., & Davis, D. S. 2008, A&A, 478, 615

Spinelli, P. F., Seitz, S., Lerchster, M., Brimioulle, F., & Finoguenov, A. 2012, MNRAS, 420, 1384

Sun, M., Voit, G. M., Donahue, M., et al. 2009, ApJ, 693, 1142

Vikhlinin, A., Burenin, R. A., Ebeling, H., et al. 2009, ApJ, 692, 1033

Vikhlinin, A., McNamara, B. R., Forman, W., et al. 1998, ApJ, 498, L21

Wright, C. O., & Brainerd, T. G. 2000, ApJ, 534, 34

Zhang, Y.-Y., Finoguenov, A., Böhringer, H., et al. 2007, Heating versus Cooling in Galaxies and Clusters of Galaxies, 60

Zhao, D. H., Jing, Y. P., Mo, H. J., Boerner, G. 2009, ApJ, 707, 354